Frictional shear thickening in suspensions: The effect of rigid asperities.

Adam K. Townsend and Helen J. Wilson
Department of Mathematics, University College London, Gower Street, London WC1E 6BT.
(Dated: September 17, 2017)

We study non-Brownian suspensions under steady shear flow. In concentrated suspensions, we are trying to reproduce the shear thickening phenomenon seen in, for example, cornstarch. We investigate the effect of different frictional contact models. When contact acts to impose a fixed minimum separation between particles, there is a strict upper bound to the viscosity predicted by simulations. We deduce that soft or compressible contacts are a critical component of the strong shear thickening seen in experiments.

PACS numbers: 83.80.Hj,83.60.Rs,46.55.+d
Keywords: shear thickening, simulation, contact, soft contact, friction

I. INTRODUCTION: SHEAR THICKENING AND CONTACT

Most common complex fluids – whether solids suspensions or polymer solutions – have viscosities, η, which decrease with shear rate, $\dot{\gamma}$: they shear thin. Some starch suspensions, including cornstarch, show the opposite behaviour: their observed steady shear viscosity increases with an increase in the imposed shear rate. Note that although starch is a polymer, a cornstarch and water mixture may be treated as a suspension of solid particles: figure 1 shows a micrograph of cornstarch, in which the separate grains of starch can clearly be seen.

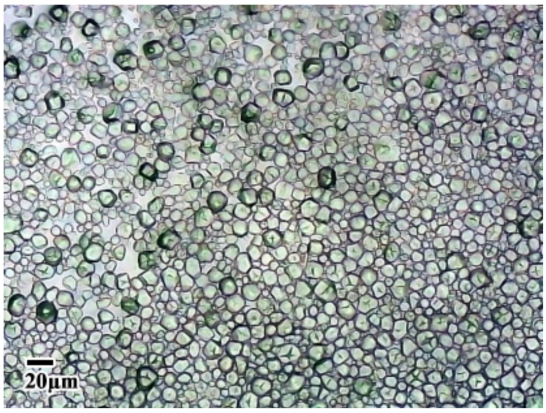

FIG. 1. Micrograph of cornstarch suspension. Courtesy of Peter Kilbride at Asymptote.

Though we can not yet predict when shear thickening will occur (not all starch solutions exhibit shear thickening [1]) there is a growing understanding of the mechanism behind it. A thorough review of the area is given by Wyart & Cates [2]; broadly, it is agreed that shear thickening occur in two forms. In **continuous shear thickening** (CST), which occurs at moderate suspension concentrations (solids volume fraction $\phi \approx 0.5$), the observed steady viscosity increases smoothly with shear rate. The viscosity increase here is relatively large – in figure 2 we see an example where the viscosity doubles during CST – but not extreme. In **discontinuous shear thickening** (DST), on the other hand, the viscosity increase is both sudden and large: in figure 2 we see that at a solids volume fraction $\phi = 0.58$, the viscosity increases by an order of magnitude as the dimensionless shear rate is changed slightly.

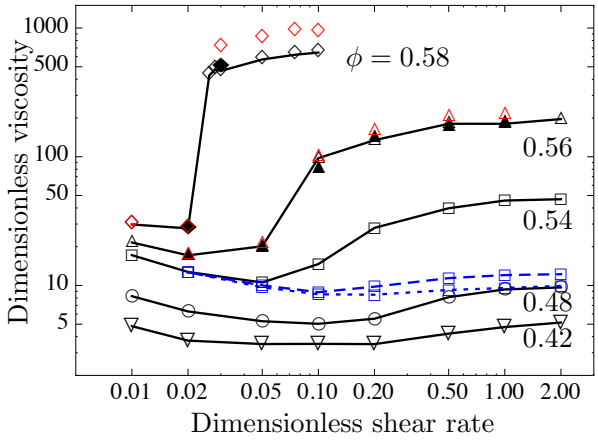

FIG. 2. Continuous and discontinuous shear thickening is observed here at varying volume concentrations (ϕ). Graph reproduced from [3] with permission.

Over the past few years, shear thickening, and particularly DST, has been the focus of sustained research effort, and we are now approaching a real understanding of the physical mechanisms behind it. In the absence of any inter-particle interactions, a pure non-Brownian suspension in Stokes flow has a constant viscosity independent of the imposed shear rate (by the linearity of Stokes flow) so we know that inter-particle interactions are important. Shear thickening is not typically seen in attractive particle solutions [4]: a repulsive inter-particle force is a key ingredient to shear thickening.

Early proposed mechanisms for DST had serious weaknesses. For instance, a mechanism built around the flow-induced formation of particle clusters [5] fails to predict viscosity jumps of the required magnitude [4]; and a proposal based around dilatancy, the tendency of granular materials to expand under flow, [6] incorrectly predicts

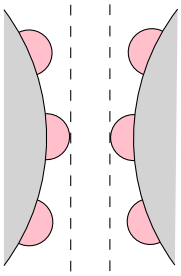

FIG. 3. Schematic of a roughness model. The pink bumps represent sparse surface asperities, which prevent the particles from approaching closer than a nominal roughness height while leaving hydrodynamic forces unchanged.

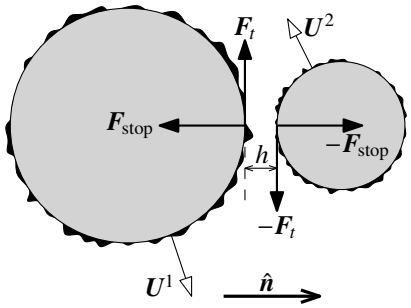

FIG. 4. The normal contact force, $\boldsymbol{F}_{\text{stop}}$, and tangential friction force, $\boldsymbol{F}_t$, oppose the motion of the approaching particles. These forces are added to any existing forces – hydrodynamic, gravity, etc. – already acting on the particles.

DST for smooth, hard particles [2].

The current consensus is that DST arises from *frictional contact* between particles [3, 7, 8], which can effectively trigger granular-type behaviour [9]. At a certain shear rate and for high enough concentrations, the forces keeping particles apart are overcome, and particles which are not perfectly smooth can come into contact. This has been confirmed in experiment [10–12]. Gallier *et al.* compile a number of experimental and simulation measurements of the effective viscosity of suspensions in figure 9 of [13], and show that frictionless simulations underestimate suspension viscosity at higher concentrations; they show that at the highest concentrations and friction coefficients, up to 70% of the viscous dissipation in simulations comes directly from contact.

The idea of contact between particles in viscous flow is not new: it follows experimental evidence of contact over the last 40 years [14, 15]. A typical roughness height for supposedly smooth particles used in suspension experiments is 5×10^{-3} of the particle radius [16, 17]: though small, this is sufficient to break symmetry in many flows and cause observable effects. Perfectly smooth spheres under finite forcing can never make contact within Stokes flow; so various models have been proposed in which microscopic surface asperities make contact while the particles' nominal surfaces are still separated by a layer of fluid. Figure 3 sketches the idea of these models: the microscopic roughness elements are assumed not to interact with the hydrodynamics of the flow, but rather to affect the particle motion directly via contact forces.

A variety of models have been used, including pure repulsion [18], stick–rotate [19] and roll–slip [19, 20]. The first of these applies no tangential force; in the second, the particles 'weld together' and cannot even roll relative to one another while the contact endures. In the roll–slip and stick–slide models, a tangential friction force is applied limited by Coulomb's law; the model of [20] implements different friction coefficients for rolling and slipping contact.

When these early models were proposed and used in simple flow situations, the idea was that the asperities would prevent the particles from approaching beyond the nominal roughness height. However, this has always been difficult to implement in large simulations. Different groups have used different forms of repulsive force when the asperity regions overlap, to imitate hard contact: a linear spring force [3, 21–23]; a Hertz contact force [13]; a dashpot force proportional to the normal approach velocity [21]; or an exponentially decaying short-range repulsive force [3, 24]. Although these force laws repel close particles, particles are still able to approach within the 'asperity contact' region. This has the effect of 'softening' roughness under strong shear.

In this paper, we exploit the linearity of Stokes flow and of the Stokesian Dynamics method to determine the required normal contact force exactly. We carry out simulations in which particles cannot approach closer than the nominal contact height; we will see that this has the effect of destroying the DST observed in simulations elsewhere.

II. IMPLEMENTATION

A. Contact model

In common with all the current DST simulations, the contact forces we apply to our particles will act only at the point of contact. We decompose the contact force into its normal component, $\boldsymbol{F}_{\text{stop}}$, and tangential component, $\boldsymbol{F}_t$. Figure 4 shows how the forces are applied to each particle. The two tangential forces also result in a torque $\boldsymbol{T} = a_i \hat{\boldsymbol{n}} \times \boldsymbol{F}_t$ being applied to each particle (with a_i the radius of the particle in question).

We now need to select the forms of $\boldsymbol{F}_{\text{stop}}$ and $\boldsymbol{F}_t$. In earlier work [25–27] we used the roll–slip model of Davis [19]. Its concept is very simple: the repulsive normal force $\boldsymbol{F}_{\text{stop}}$ is precisely chosen to prevent particle approach beyond a critical surface separation h, and the tangential force $\boldsymbol{F}_t$ resists the relative tangential motion of the particle surfaces, and is limited in magnitude by $\nu|\boldsymbol{F}_{\text{stop}}|$, where ν is a friction coefficient. For dilute suspensions [25], increasing the roughness height lowers the

suspension viscosity by increasing the inter-particle gap and thereby lowering lubrication dissipation; and increasing the friction coefficient increases the viscosity very mildly. However, shear thickening only occurs in suspensions which are far from dilute. In later work ([26], corrected in [27]), we carried out small simulations of concentrated suspensions in shear flow; here, increasing either the roughness height or the friction coefficient tended to increase the viscosity. There were two major weaknesses of this study, however (beside the small size of the simulations, which is simply a measure of the computational power available in 2002). We determined $\boldsymbol{F}_{\rm stop}$ using an iterative algorithm, which failed to converge for highly concentrated suspensions, so we were limited in our scope. More fundamental, however, for the purpose of shear thickening: all the forces in this model are linear in the external flow forcing, so *the viscosity is independent of shear rate*. In order to reproduce any shear thickening effects, we need the friction force to vary in a nonlinear way with the external forcing.

This is accomplished, as in Seto *et al.* [3], Mari *et al.* [21] for example, using a critical load model. The frictional tangential force, $\boldsymbol{F}_t$, is now only applied if the magnitude of the normal force, $|\boldsymbol{F}_{\rm stop}|$, exceeds a critical value $F_{\rm crit}$. The concept of the critical load model is drawn from granular flows; following its success in simulations, there is recent experimental evidence [11, 12] that suspensions are indeed frictionless when the compressive forces acting are small. This modification to the model brings the possibility of shear thickening: at low flow rates, the normal forces are small and the tangential forces are never imposed; at higher flow rates, there is a frictional contribution to the dissipation which increases the overall viscosity.

Our final model has three parameters: the critical separation distance h, which has typical values [16]

$$10^{-3} \leq \frac{h}{(a_1+a_2)/2} \leq 10^{-2}, \tag{1}$$

the coefficient of friction ν, which has typical values [15]

$$0.1 \leq \nu \leq 0.4, \tag{2}$$

and the critical load $F_{\rm crit}$, which is used to set a timescale

$$T_{\rm crit} = \frac{6\pi\mu a^2}{F_{\rm crit}} \tag{3}$$

against which the shear rate will be made dimensionless.

The process for calculating the contact forces is as follows:

1. Using velocities from the previous timestep, identify any new contacting pairs: that is, approaching pairs of particles whose surfaces are within the critical separation h. Add these to the list of contacting pairs.

2. Calculate the normal forces, $\boldsymbol{F}_{\rm stop}$, required to keep the interparticle separation of each listed contacting particle pair unchanged.

3. Remove from the contact list any pairs of particles for which $\boldsymbol{F}_{\rm stop}$ acts to pull the particles together: only repulsive forces can be exerted by contact.

4. For those remaining pairs for which $|\boldsymbol{F}_{\rm stop}| < F_{\rm crit}$, the contact force is simply $\boldsymbol{F}_{\rm stop}$, with no tangential component.

5. For those pairs for which $|\boldsymbol{F}_{\rm stop}| > F_{\rm crit}$, we impose $\boldsymbol{F}_{\rm stop}$ as the normal component of the contact force. Next calculate the tangential force $\boldsymbol{F}_{\rm roll}$ required to prevent slipping between the particle surfaces.

6. For each such pair, check whether $|\boldsymbol{F}_{\rm roll}| > \nu|\boldsymbol{F}_{\rm stop}|$.

$$\begin{aligned} &\text{If } |\boldsymbol{F}_{\rm roll}| > \nu|\boldsymbol{F}_{\rm stop}|, \text{ then set } \ \boldsymbol{F}_t = \nu|\boldsymbol{F}_{\rm stop}|\frac{\boldsymbol{F}_{\rm roll}}{|\boldsymbol{F}_{\rm roll}|}. \\ &\text{If } |\boldsymbol{F}_{\rm roll}| \leq \nu|\boldsymbol{F}_{\rm stop}|, \text{ then set } \ \boldsymbol{F}_t = \boldsymbol{F}_{\rm roll}. \end{aligned} \tag{4}$$

At step 2, we need to determine the normal forces required to prevent particle approach. We do this by exploiting the linearity of our simulation framework, Stokesian Dynamics. Recall that for a timestep without contact forces, in a linear background flow field

$$\boldsymbol{u}^\infty(\boldsymbol{x}) = \boldsymbol{U}^\infty + \boldsymbol{\Omega}^\infty \times \boldsymbol{x} + \boldsymbol{E}^\infty \cdot \boldsymbol{x}, \tag{5}$$

the Stokesian Dynamics method consists of solving the linear system

$$\begin{pmatrix} \boldsymbol{F}^1 \\ \boldsymbol{F}^2 \\ \vdots \\ \boldsymbol{T}^1 \\ \boldsymbol{T}^2 \\ \vdots \\ \boldsymbol{S}^1 \\ \boldsymbol{S}^2 \\ \vdots \end{pmatrix} = \mathcal{R} \begin{pmatrix} \boldsymbol{U}^1 - \boldsymbol{u}^\infty(\boldsymbol{x}^1) \\ \boldsymbol{U}^2 - \boldsymbol{u}^\infty(\boldsymbol{x}^2) \\ \vdots \\ \boldsymbol{\Omega}^1 - \boldsymbol{\Omega}^\infty \\ \boldsymbol{\Omega}^2 - \boldsymbol{\Omega}^\infty \\ \vdots \\ -\boldsymbol{E}^\infty \\ -\boldsymbol{E}^\infty \\ \vdots \end{pmatrix}, \tag{6}$$

in which $\boldsymbol{F}^i$ and $\boldsymbol{T}^i$ are any other external forces and torques acting on sphere i, $\boldsymbol{u}^\infty(\boldsymbol{x})$ and $\mathcal{R}$ is the Stokesian Dynamics approximation [5] to the grand resistance matrix, formed from exact two-sphere resistance relations for $\mathcal{R}^{\rm 2B}$ and Faxén laws for the far-field mobility relations:

$$\mathcal{R} = (\mathcal{M}^\infty)^{-1} + \mathcal{R}^{\rm 2B} - \mathcal{R}^{\rm 2B,\infty}. \tag{7}$$

Here we are using $\boldsymbol{U}^i$ to denote the velocity of sphere i and $\boldsymbol{\Omega}^i$ its rotational velocity. The stresslet $\boldsymbol{S}^i$ is generated by particle i.

Now suppose that particles 1 and 2 are in close approach. The normal stopping force on particle 1 can be written

$$\boldsymbol{F}_{\rm stop} = -F^{12}_{\rm stop}\hat{\boldsymbol{n}}^{12}, \tag{8}$$

where $\widehat{\boldsymbol{n}}^{12}$ is the unit vector along the line of centres between the particles at positions $\boldsymbol{r}^1$ and $\boldsymbol{r}^2$:

$$\widehat{\boldsymbol{n}}^{12} = \frac{\boldsymbol{r}^2 - \boldsymbol{r}^1}{|\boldsymbol{r}^2 - \boldsymbol{r}^1|}. \tag{9}$$

An equal and opposite force, $-\boldsymbol{F}_{\text{stop}}$, is placed on particle 2. The condition for stopping this pair approaching is that

$$(\boldsymbol{U}^2 - \boldsymbol{U}^1) \cdot \widehat{\boldsymbol{n}}^{12} = 0. \tag{10}$$

We can then write the resistance formulation of this new system as

$$\begin{pmatrix} \boldsymbol{F}^1 - F^{12}_{\text{stop}}\widehat{\boldsymbol{n}}^{12} \\ \boldsymbol{F}^2 + F^{12}_{\text{stop}}\widehat{\boldsymbol{n}}^{12} \\ \boldsymbol{T}^1 \\ \boldsymbol{T}^2 \\ \boldsymbol{S}^1 \\ \boldsymbol{S}^2 \end{pmatrix} = \mathcal{R} \begin{pmatrix} \boldsymbol{U}^1 - \boldsymbol{u}^\infty(\boldsymbol{x}^1) \\ \boldsymbol{U}^2 - \boldsymbol{u}^\infty(\boldsymbol{x}^2) \\ \boldsymbol{\Omega}^1 - \boldsymbol{\Omega}^\infty \\ \boldsymbol{\Omega}^2 - \boldsymbol{\Omega}^\infty \\ -\boldsymbol{E}^\infty \\ -\boldsymbol{E}^\infty \end{pmatrix}. \tag{11}$$

We can combine equations (10–11) into a single matrix equation:

$$\left(\begin{array}{c} \boldsymbol{F}^1 \\ \boldsymbol{F}^2 \\ \hline \widehat{\boldsymbol{n}}^{12} \cdot [\boldsymbol{u}^\infty(\boldsymbol{x}^2) - \boldsymbol{u}^\infty(\boldsymbol{x}^1)] \end{array}\right) = \left(\begin{array}{cc|c} & & \widehat{\boldsymbol{n}}^{12} \\ \multicolumn{2}{c|}{\mathcal{R}} & -\widehat{\boldsymbol{n}}^{12} \\ \hline \widehat{\boldsymbol{n}}^{12} & -\widehat{\boldsymbol{n}}^{12} & 0 \end{array}\right) \left(\begin{array}{c} \boldsymbol{U}^1 - \boldsymbol{u}^\infty(\boldsymbol{x}^1) \\ \boldsymbol{U}^2 - \boldsymbol{u}^\infty(\boldsymbol{x}^2) \\ \hline F^{12}_{\text{stop}} \end{array}\right), \tag{12}$$

where, for clarity, the torque and stresslet terms (and rows and columns relating to other particles) have been omitted. An extra row and column is added to the resistance matrix for every contacting pair. For example, for three particles, where only 1–2 and 2–3 are in contact, we have

$$\left(\begin{array}{c} \boldsymbol{F}^1 \\ \boldsymbol{F}^2 \\ \boldsymbol{F}^3 \\ \hline \widehat{\boldsymbol{n}}^{12} \cdot [\boldsymbol{u}^\infty(\boldsymbol{x}^2) - \boldsymbol{u}^\infty(\boldsymbol{x}^1)] \\ \widehat{\boldsymbol{n}}^{23} \cdot [\boldsymbol{u}^\infty(\boldsymbol{x}^3) - \boldsymbol{u}^\infty(\boldsymbol{x}^2)] \end{array}\right) = \left(\begin{array}{ccc|cc} & & & \widehat{\boldsymbol{n}}^{12} & \boldsymbol{0} \\ & \mathcal{R} & & -\widehat{\boldsymbol{n}}^{12} & \widehat{\boldsymbol{n}}^{23} \\ & & & \boldsymbol{0} & -\widehat{\boldsymbol{n}}^{23} \\ \hline \widehat{\boldsymbol{n}}^{12} & -\widehat{\boldsymbol{n}}^{12} & \boldsymbol{0} & \multicolumn{2}{c}{\multirow{2}{*}{$\boldsymbol{0}$}} \\ \boldsymbol{0} & \widehat{\boldsymbol{n}}^{23} & -\widehat{\boldsymbol{n}}^{23} & \multicolumn{2}{c}{} \end{array}\right) \left(\begin{array}{c} \boldsymbol{U}^1 - \boldsymbol{u}^\infty(\boldsymbol{x}^1) \\ \boldsymbol{U}^2 - \boldsymbol{u}^\infty(\boldsymbol{x}^2) \\ \boldsymbol{U}^3 - \boldsymbol{u}^\infty(\boldsymbol{x}^3) \\ \hline F^{12}_{\text{stop}} \\ F^{23}_{\text{stop}} \end{array}\right). \tag{13}$$

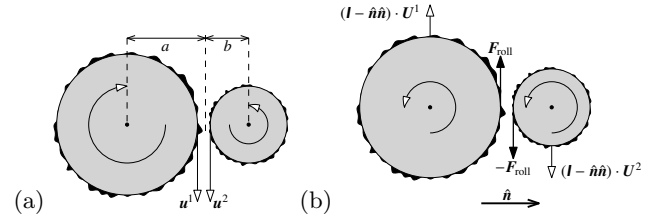

FIG. 5. Rolling contact between two spheres. (a) The velocities at the contact point need to be equal for rolling. (b) Small test case to determine the required tangential force.

We have retained the symmetry, and positive definiteness, of the matrix system, and we can calculate the scalars F^{ij}_{stop} with very little extra computational effort.

In step 5 of our process, we need to calculate the tangential force required for rolling contact between a given pair of spheres. Rolling contact occurs when the tangential velocities of the particle surfaces, at the point of contact, are equal (see figure 5(a)). We do this using lubrication theory, along with the particle velocities calculated in the presence only of normal forces.

For spheres where the centre-to-contact distances are a and b, the tangential velocities on the surface are

$$\boldsymbol{u}^1_t = (\boldsymbol{I} - \widehat{\boldsymbol{n}}\widehat{\boldsymbol{n}}) \cdot \boldsymbol{U}^1 + \boldsymbol{\Omega}^1 \times a\widehat{\boldsymbol{n}}, \tag{14}$$

$$\boldsymbol{u}^2_t = (\boldsymbol{I} - \widehat{\boldsymbol{n}}\widehat{\boldsymbol{n}}) \cdot \boldsymbol{U}^2 + \boldsymbol{\Omega}^2 \times (-b\widehat{\boldsymbol{n}}), \tag{15}$$

and the tangential velocity difference (which we want to force to be zero) is

$$\boldsymbol{u}^2_t - \boldsymbol{u}^1_t = (\boldsymbol{I} - \widehat{\boldsymbol{n}}\widehat{\boldsymbol{n}}) \cdot (\boldsymbol{U}^2 - \boldsymbol{U}^1) - (a\boldsymbol{\Omega}^1 + b\boldsymbol{\Omega}^2) \times \widehat{\boldsymbol{n}}. \tag{16}$$

Now consider the small test case shown in figure 5(b). We apply the tangential force $\boldsymbol{F}_{\text{roll}}$ to particle 1, and the corresponding force $-\boldsymbol{F}_{\text{roll}}$ to particle 2; these also result in torques applying to each particle. The resultant motion can be described by the equation

$$\begin{pmatrix} (\boldsymbol{I} - \widehat{\boldsymbol{n}}\widehat{\boldsymbol{n}}) \cdot \boldsymbol{U}^1 \\ (\boldsymbol{I} - \widehat{\boldsymbol{n}}\widehat{\boldsymbol{n}}) \cdot \boldsymbol{U}^2 \\ \boldsymbol{\Omega}^1 \\ \boldsymbol{\Omega}^2 \end{pmatrix} = \mathcal{M} \begin{pmatrix} \boldsymbol{F}_{\text{roll}} \\ -\boldsymbol{F}_{\text{roll}} \\ \widehat{\boldsymbol{n}}a \times \boldsymbol{F}_{\text{roll}} \\ \widehat{\boldsymbol{n}}b \times \boldsymbol{F}_{\text{roll}} \end{pmatrix}. \tag{17}$$

where $\mathcal{M}$ is the two-sphere mobility matrix [28]. We can write the new tangential velocity difference, using the mobility scalars of Kim [28], as

$$\begin{aligned} \boldsymbol{u}^2_t - \boldsymbol{u}^1_t = \big[& -(y^{11}_a - y^{12}_a - y^{21}_a + y^{22}_a) \\ & + 2(ay^{11}_b - ay^{12}_b + by^{21}_b - by^{22}_b) \\ & - (a^2 y^{11}_c + aby^{12}_c + aby^{21}_c + b^2 y^{22}_c) \big] \boldsymbol{F}_{\text{roll}}, \end{aligned} \tag{18}$$

which gives us $\boldsymbol{F}_{\text{roll}}$ if we know the mobility scalars.

For close spheres, the leading order terms of these mobility scalars can be written in terms of the sphere surface separation distance, $\xi = 2r/(a+b) - 2$ [28, tables 11.17 and 11.21]. In particular, for equal-sized spheres, $a = b$, this reduces the above equation to

$$\boldsymbol{F}_{\text{roll}} = \frac{\pi\mu a(\ln\xi - 6.04 + 6.33/\ln\xi)}{1 - 4.69/\ln\xi} \times \left[(\boldsymbol{I} - \hat{\boldsymbol{n}}\hat{\boldsymbol{n}}) \cdot (\boldsymbol{U}^2 - \boldsymbol{U}^1) - a(\boldsymbol{\Omega}^1 + \boldsymbol{\Omega}^2) \times \hat{\boldsymbol{n}}\right], \quad (19)$$

as in Wilson and Davis [26, eq. 3.2].

We have not implemented a more sophisticated friction model such as the stick–slide model of Mari *et al.* [21], which uses tangential spring stretch, a concept borrowed from granular dynamics. Instead, we are making as small a deviation as possible from the early models for simplicity.

Though we are describing this implementation as an exact calculation, in reality there are still small approximations involved. Regarding the normal forces: what we have actually calculated is the set of normal forces required to *simultaneously* halt the normal motion of all contacting pairs *in the absence of tangential forces*. Once the normal forces for those pairs which are observed to need an attractive $\boldsymbol{F}_{\text{stop}}$ are removed, and tangential forces are added, these remaining normal contact forces will no longer perfectly prevent particle approach. However, it is reasonable to use them. The first modification – the removal of the normal forces for those pairs which are separating – is a rare event (it occurs only when a pair which has been in compressive contact moves out of it) and also a small change (the normal velocities, and hence the normal force, are very small at this point). The second modification is more common, but still only occurs when $|\boldsymbol{F}_{\text{stop}}| > F_{\text{crit}}$; and the magnitude of the added force is at most $\nu|\boldsymbol{F}_{\text{stop}}|$. Since we limit ourselves to physically realistic values $\nu < 1$, the added forces are at least constrained to be smaller than the normal forces we claim to calculate exactly. In figure 6 we show the mean approach velocity of all contacting pairs for a variety of simulations; in all cases they are of the order of 10^{-3} or smaller.

The tangential forces are calculated via the lubrication approximation. One might wonder why we do not implement something similar to equation (13) in order to produce an exact value for $\boldsymbol{F}_{\text{roll}}$. However, if we did that we would end up with the set of tangential forces $\boldsymbol{F}_{\text{roll}}$ required to *simultaneously cause rolling motion of all pairs in which friction is activated*. In figure 7 we plot the time-averaged numbers of particle pairs in each state (contact; friction-activated contact; slipping motion (tangential force limited by friction); or rolling motion), for simulations at an area fraction of 69%. As expected, the proportion of friction-activated particles which roll increases with increasing ν; at $\nu = 0.1$ roughly half the friction-activated particles are in rolling contact. At $\nu = 0.4$ a much higher proportion are in rolling motion, and perhaps we might find our tangential forces more accurately by using an exact method; but it should be borne in mind that the lubrication approximation is also reasonably accurate at these small surface separations.

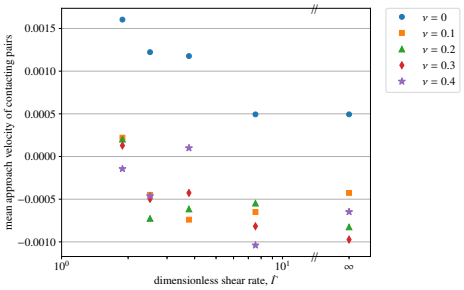

FIG. 6. Mean approach velocity (across all contacting pairs) for simulations with different values of ν and $\dot{\Gamma}$. All values are at most of magnitude 10^{-3}, which is rather small, so we can conclude that our normal forces are indeed a good approximation to those which exactly halt particle approach. There is no systematic dependence on either friction coefficient or shear rate; these values are just small-magnitude noise.

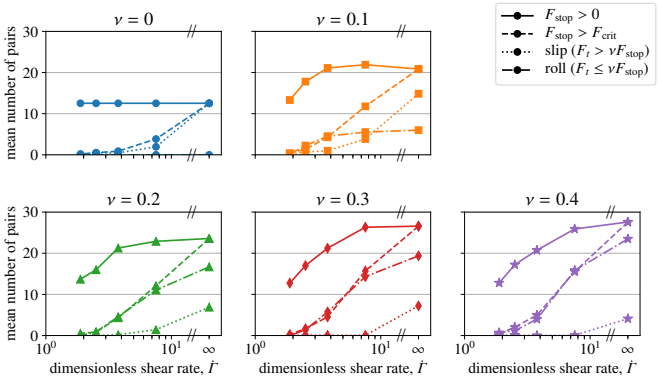

FIG. 7. Information about the number of particle pairs in contact; in friction-activated contact; in rolling contact; and in slipping contact. Simulation parameters $c = 0.69$, $h = 0.01a$.

B. Simulation protocol

For the bulk of the results in this paper, we simulate the motion of a single plane of identical spheres of radius a within an infinite volume of viscous fluid of viscosity μ. We use a periodic box of area A, and impose a shear flow in the plane of the particles, with shear rate $\dot{\gamma}$.

Because we just have one plane of particles, the volume concentration is strictly zero: but because the spheres all reside in the plane of shear, they interact strongly with one another, and the effects of contact can be felt. The extra viscosity contributed by the particles can be extracted from Stokesian Dynamics simulations via the particle stresslets $\boldsymbol{S}$, and in particular their shear components. For a 3D simulation with solid volume fraction

ϕ in a volume V, we would have the effective viscosity

$$\eta = \mu + \frac{1}{\dot{\gamma} V} \sum_{\alpha} S_{12}^{\alpha}, \tag{20}$$

(where the summation is over all particles α) which leads, for well-separated spheres for which

$$\boldsymbol{S}^{\alpha} = \frac{20}{3}\pi\mu a^3 \boldsymbol{E}^{\infty} \qquad S_{12}^{\alpha} = \frac{10}{3}\pi\mu a^3 \dot{\gamma}, \tag{21}$$

to the Einstein relation [29]:

$$\eta = \mu\left(1 + \frac{5}{2}\phi\right). \tag{22}$$

For a single plane of spheres, we follow the convention established by Brady and Bossis [30] and take the nominal width of the layer to be the particle diameter, $2a$. Then our region of area A has volume $V = 2aA$. If we define the area fraction as c, the equivalent of equation (22) becomes

$$\eta = \mu\left(1 + \frac{5}{3}c\right). \tag{23}$$

This formula also gives a lower bound for the effective viscosity, using the minimum dissipation theorem.

We will report our viscosity results in terms of the dimensionless effective viscosity η/μ and the dimensionless shear rate

$$\dot{\Gamma} = \dot{\gamma} T_{\text{crit}} = \frac{6\pi\mu\dot{\gamma}a^2}{F_{\text{crit}}}, \tag{24}$$

notated $\dot{\Gamma}$ to match the literature, which is analogous to the Péclet number. Shear thickening has been seen to occur for $\dot{\Gamma}$ above 10^{-1} [13]; we will consider shear rates in the region $10^0 < \dot{\Gamma} < 10^2$.

There is a popular modification to Stokesian Dynamics, now in common use for very concentrated suspensions [e.g. 21, 31], which involves neglecting the two-particle interactions in the grand mobility matrix $\mathcal{M}^{\infty}$ and instead using the appropriate value for isolated spheres. We will use this – referred to as the Ball–Melrose approximation – in some of our larger simulations; we will also discuss the effect it has on the macroscopic viscosity measurements.

III. VERIFICATION

We are using our own new implementation of Stokesian Dynamics, which has been extensively verified against results from both the original code of Brady and Bossis [5] and the more recent (and independent) implementation of Wilson and Davis [26]. The only aspect remaining to be fully checked for the current work is the implementation of the contact force. We confirm that the contact force is working as expected using studies of just two close spheres.

Our test scenario, shown in figure 8, is the motion of two passing spheres. These equisized particles have equal and opposite external forces imposed upon them, in a quiescent fluid. We apply horizontal forces $\widehat{\boldsymbol{e}}_x$ and $-\widehat{\boldsymbol{e}}_x$ to spheres whose initial positions are $(-5a, 0.25a)$ and $(5a, -0.25a)$ respectively. The particles then move in time and the positions of their centres are shown. We see that contact causes an increased offset downstream relative to upstream, as expected. Other effects of the increased minimum separation are to lessen the interaction between the particles: so they travel further than they would in the absence of contact, and rotate less. The addition of friction primarily affects the rotation: at a realistic friction coefficient of $\nu = 0.5$, the particles rotate a similar angle to the contact-free situation.

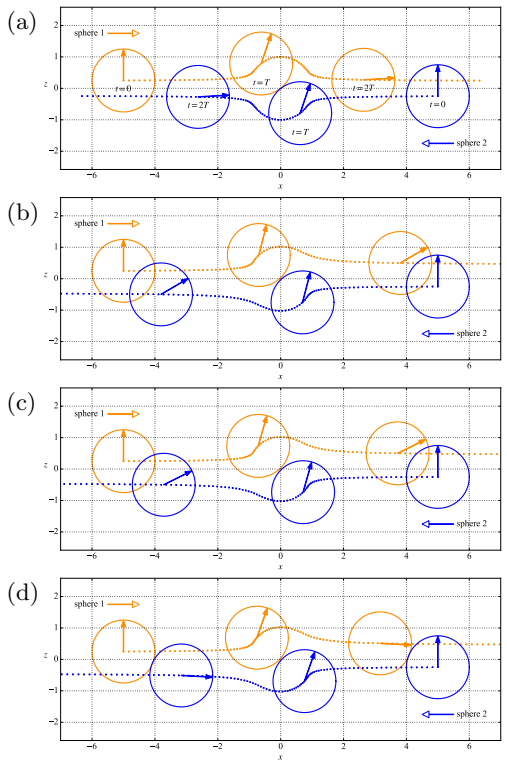

FIG. 8. The effect of contact forces on two spheres passing under external forcing. The circles indicate the position of the particle at three evenly spaced times. The arrows in the circles indicate the orientation of the particles, which always start upright. The dotted lines indicate the path of the particle centres; the dots are spaced at regular time intervals. (a) No contact: the trajectories are fore-aft symmetric, and both particles rotate by almost 90° during their interaction. (b) Normal contact force only (no friction); critical roughness height $h = 0.05a$. The fore-aft symmetry is destroyed by contact, and the rotation of both particles is reduced. The particles also travel further than when contact is absent. (c) Small friction coefficient, $\nu = 0.1$: very little difference from the friction-free contact case. (d) Large friction coefficient, $\nu = 0.5$. The roughness height h is chosen unphysically large here to demonstrate the effect of contact, and we have set the critical load $F_{\text{crit}} = 0$.

We have also carried out similar simulations using two spheres of very different sizes. In all cases, the small sphere carries out most of the rotation, as one would expect; the other observations carry over unchanged from the equal-spheres case.

IV. SIMULATION RESULTS

We will begin by exploring the effect of various different simulation parameters, before demonstrating the effect of our contact model on the phenomenon of shear thickening. We are using simulations of a single layer of spheres, so we parametrise the particle density in terms of the area concentration c. For a monodisperse 3D suspension with volume fraction ϕ, close packing occurs at $\phi_{\mathrm{CP}} = \pi/3\sqrt{2} \approx 74\%$, while the highest freely-shearing density (consisting of non-overlapping layers of packed spheres) is $\phi_{\mathrm{FS}} = \pi/3\sqrt{3} \approx 60\%$. For a single layer of spheres, the close-packed area fraction is $c_{\mathrm{CP}} = \sqrt{3}\pi/6 \approx 91\%$ and the freely-shearing packing fraction, $c_{\mathrm{FS}} = \pi/4 \approx 79\%$. These arrangements are sketched in figure 9.

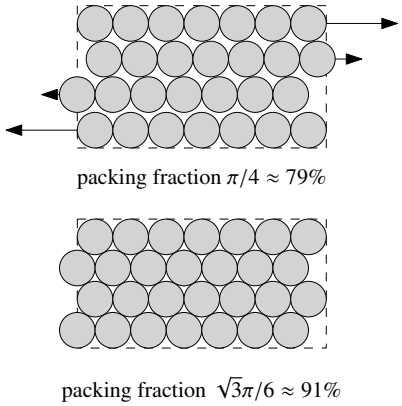

FIG. 9. Packing fractions below 79% allow for particles to shear past each other without bumping. When packing fractions approach 91%, the system jams completely.

For these two critical packing states, the key ratio c/ϕ is rather similar (between 1.2 and 1.3), so we can map conclusions from our layer simulations into 3D parameter space in a coherent way. In particular, referring back to the simulation data shown in figure 2, we see that both CST and DST are observed at packing fractions ϕ *below* the freely-shearing packing fraction, so we would expect this sort of behaviour at area fractions just below $c_{\mathrm{FS}} \approx 79\%$.

A. Simulation time

In figure 10 we plot the time-trace of the shear viscosity for two simulations at slightly lower concentrations $c = 57\%$ and 69%, to show how the system evolves in time. We can see that, while the signal remains noisy (as one would expect), the initial transients (much more visible at the higher concentration) have dissipated after two shear units.

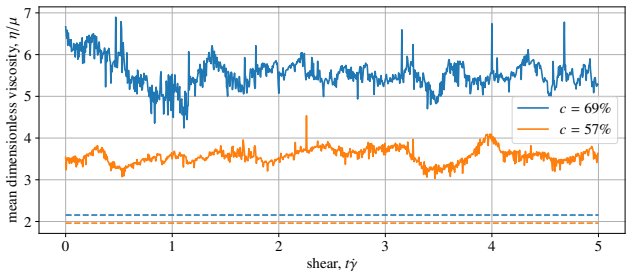

FIG. 10. Dimensionless viscosity under shear, measured over five shear units. Here the friction coefficient is $\nu = 0.3$, roughness height $h = 0.01a$, timestep $\Delta t = 5 \times 10^{-3}\dot{\gamma}^{-1}$ and the dimensionless shear rate is $\dot{\Gamma} = 6\pi$. Each periodic box contains 90 identical spheres. The dashed lines represent the dilute viscosity limit for each concentration, $1 + 5c/3$.

Henceforth we will simulate five shear units of flow for each set of parameters, discard the first two shear units of equilibration, and average over the remaining time to produce a single data point. To further reduce the effect of our initial particle placements, we also average over different initial conditions.

B. Choice of timestep

We use RK4 timestepping, and in figure 11 we carry out calculations using three different timesteps to ascertain the importance of taking Δt sufficiently small. We see that a figure of $\Delta t = 0.005/\dot{\gamma}$ is adequate to capture the qualitative features of the viscosity profile, though it systematically overestimates the true viscosity by around 5%.

C. Effect of periodic cell size

Our most significant results are likely to be at the highest concentrations we can simulate; these are, of course, also the simulations in which a periodic box containing 90 particles takes up the smallest total area – and therefore the effects of the finite replicating cell are likely to be most apparent. In figure 12 we carry out simulations at our higher concentrations (area fractions $c = 69.3\%$, 75% and 80%) using a variety of particle numbers. To make the larger simulations tractable we use the Ball–Melrose approximation here; for comparability we use it in all the calculations in figure 12.

We see that at a concentration of 69%, there is no coherent trend of viscosity measurements against box size – the differences here are simply the usual variation associated with different starting conditions – and

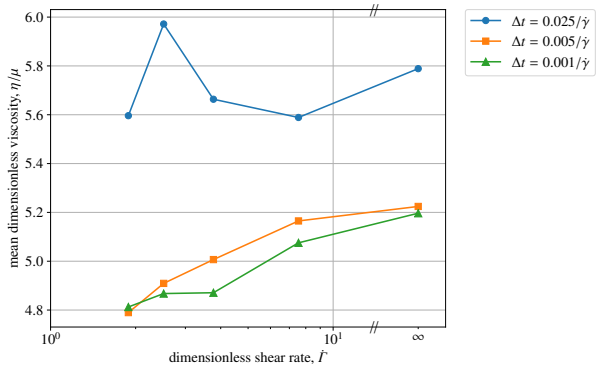

FIG. 11. The effect of varying the timestep Δt. Plot of the mean steady viscosity with model parameters $\nu = 0.3$, $h = 0.01a$, and a periodic box containing 90 spheres at an area fraction of 69.3%. A timestep $\Delta t = 0.025\dot{\gamma}^{-1}$ is too large to make meaningful predictions; but the marginal gain in accuracy by reducing from $\Delta t = 0.005\dot{\gamma}^{-1}$ to $\Delta t = 0.001\dot{\gamma}^{-1}$ does not merit the extra computational effort involved.

we can assume that 90 particles are sufficient to give a robust result. At 75% (marginally) and, more strongly, at 80% area fraction, however, we see that there is a coherent increase of viscosity with shear rate which is only seen when sufficient particles are used in the simulation. For this reason, when we report our results in the following sections, we will use larger simulations (and the Ball–Melrose approximation) at the highest concentration 80%.

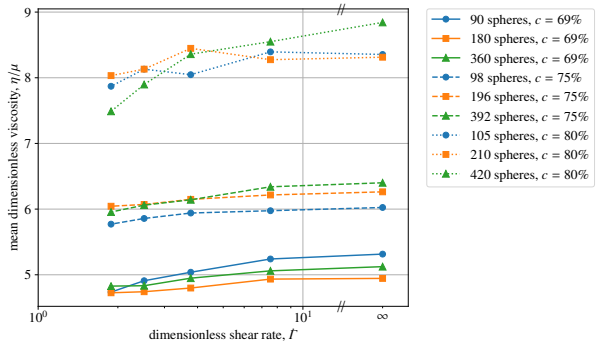

FIG. 12. The effect of system size. Model parameters $\nu = 0.3$, $h = 0.01a$, and we are using the Ball–Melrose approximation to save computation time. At the highest concentration, box size effects are important; at $c = 69\%$ 90 particles will suffice and at $c = 75\%$ we use 98 particles.

D. The Ball–Melrose approximation

Since we need to use the Ball–Melrose approximation (which replaces each instance of $\mathcal{M}^\infty$ in Stokesian Dynamics with its equivalent value for isolated spheres) at our higher concentrations, in figure 13 we show what effect it has on viscosity measurements. These calculations

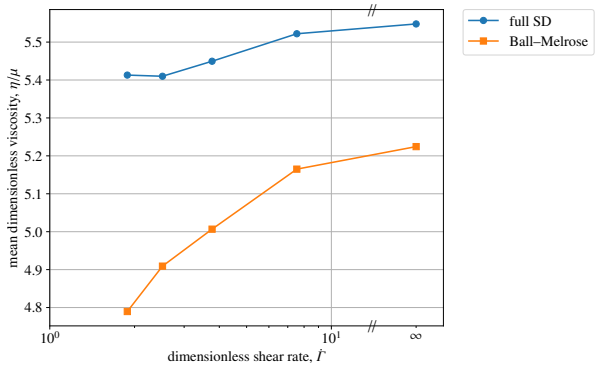

FIG. 13. Comparison of the viscosity calculated by full Stokesian Dynamics with the Ball–Melrose approximation. Simulations of 90 spheres at an area fraction $c = 69.3\%$, using $\nu = 0.3$ and $h = 0.01a$.

are carried out with only 90 spheres at an area fraction $c = 69.3\%$ as to go to higher particle numbers is computationally intractable.

We find that the viscosity predicted by full Stokesian Dynamics is 5–15% higher than that given by the Ball–Melrose approximation. Both sets of simulations shown here exhibit shear thickening, but the effect is amplified by the Ball–Melrose approximation: though the absolute viscosities are lower, the dependence on shear-rate is stronger.

E. Shear thickening results: Concentration

To see the development of shear thickening behaviour as concentration increases, we now carry out a full set of simulations at a range of values of the area fraction c, and over the full physically relevant range of the dimensionless shear rate, $\dot{\Gamma}$. The results are shown in figure 14.

At low-to-medium concentrations, we see almost no change in the viscosity as the shear rate is increased. At $c = 69\%$ we see a 3% increase in viscosity, and at $c = 80\%$, the viscosity increases by 20% as the shear rate changes. This is qualitatively similar to the CST seen in, for example, figure 2. However, the area fraction here is above the freely-shearing limit $c_{\mathrm{FS}} = \pi/4 \approx 79\%$. This is in contrast to 3D simulations in the literature [3], in which both CST and DST occur at volume fractions below the freely-shearing limit.

F. Shear thickening results: Friction coefficient

Finally, we show the dependence of our viscosity results on friction coefficient in figure 15. It is no surprise to see that on average the viscosity of the system increases with increasing ν; individual exceptions to this within the figure are simply the result of variation between simulations.

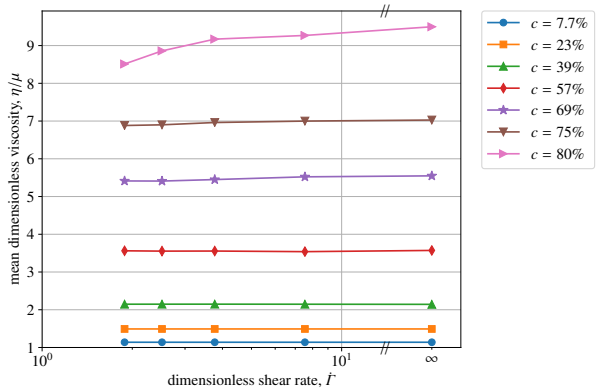

FIG. 14. Dependence of the dimensionless viscosity on dimensionless shear rate at different values of the area fraction c. At concentrations up to 69% we use full Stokesian Dynamics with 90 particles; at 75% we use 98 particles; and at the highest concentration we use the Ball–Melrose approximation to allow us to use more particles. The model parameters are $h = 0.01a$ and $\nu = 0.3$.

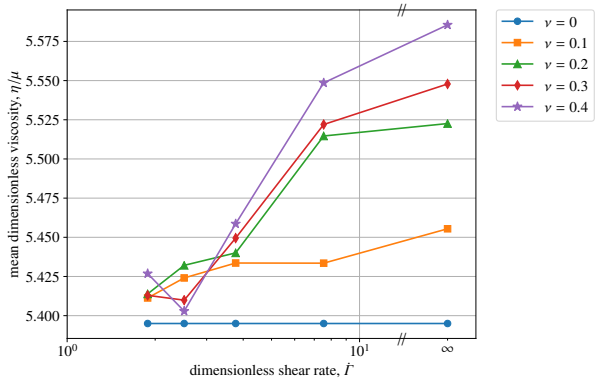

FIG. 15. Plot of dimensionless viscosity against dimensionless shear rate for a system with area fraction $c = 69.3\%$, $h = 0.01a$ and a range of values of the friction coefficient ν. There are 90 particles in the periodic cell and we are using full Stokesian Dynamics.

The shear thickening here is very moderate, and this is an inevitable result of our choice of contact model. Because the dimensionless shear rate is defined as

$$\dot{\Gamma} = \dot{\gamma} T_{\text{crit}} = \frac{6\pi\mu\dot{\gamma}a^2}{F_{\text{crit}}}, \tag{25}$$

the limit $\dot{\Gamma} \to 0$ corresponds to $F_{\text{crit}} \to \infty$, in which the tangential friction forces never apply: this is equivalent to setting $\nu = 0$. On the other hand, the limit $\dot{\Gamma} \to \infty$ corresponds to setting $F_{\text{crit}} = 0$, and applying the tangential friction force to all contacting pairs. This is the original roll-slip model of [19], which generates only small variations of viscosity with friction coefficient [26, 27].

This conclusion is wider than the specific combination of contact models introduced here. Another common method of introducing flow-rate dependence into suspension flow is to incorporate a short-range repulsive force between particles, separate from the contact force (as in [32]). At low flow rates, this makes contact unlikely, while at higher flow rates the driving flow overcomes the repulsive force and the contact occurs almost unaffected. However, in the limit of very fast flow, the physical interactions are reduced to the case of no repulsive force: again, the maximum possible shear viscosity is that predicted by the original roll-slip contact model alone.

G. Shear thickening results: Shear rate

In all the graphs we have plotted in the preceding sections (with the exception of those for which $\nu = 0$, where no thickening is observed), we see viscosity as an increasing function of the shear rate $\dot{\Gamma}$, but the experimentally-observed plateaus in the viscosity at high and low shear rates are not necessarily obvious. This is simply because we have only plotted over the range of shear rates where interesting behaviour occurs.

At low shear rates, we have $\dot{\Gamma} \ll 1$, or equivalently $F_{\text{crit}} \gg 6\pi\mu a^2\dot{\gamma}$. Large values of F_{crit} result in a form of contact in which friction is never activated: so the viscosity at lower shear rates is not sensitively dependent on the shear rate, but reduces to the value predicted by our model (at all shear rates) when $\nu = 0$.

At high shear rates, on the other hand, we have $\dot{\Gamma} \gg 1$, and so $F_{\text{crit}} \ll 6\pi\mu a^2\dot{\gamma}$. The typical stress in the system is now much larger than F_{crit}, so most contacting pairs will experience frictional contact. In the limit of very high shear rates, the system is equivalent to setting $F_{\text{crit}} = 0$, which is precisely the original frictional contact model of Davis [19]. We have included this data point on the results graphs, labelled as $\dot{\Gamma} = \infty$.

The viscosity is, therefore, an increasing function of shear rate which is bounded below by the Davis model with $\nu = 0$ (the pure hard-sphere repulsion model) and above by the Davis model with the appropriate value of ν. Generically, it must have plateaus at low and high shear rates with an increasing region between. In this paper we have focused only on the increasing region.

V. CONCLUSIONS

We have used Stokesian Dynamics to simulate shear flow of a suspension of identical rough particles with frictional contact between them, in an attempt to replicate shear thickening. We have also quantified the effect of the Ball–Melrose approximation, in which far-field interactions are approximated by their value for isolated particles; it is shown to underpredict the shear viscosity of the suspension while also overpredicting the shear thickening effect (that is, the underprediction is worse at low shear rates).

Many authors have used a range of different models of particle contact in order to capture the phenomenon of

shear thickening. For the first time, we have produced an accurate implementation for a set of models for which contact halts the approach of a particle pair.

At high enough particle concentrations, this model can lead to shear-thickening behaviour in suspensions; however, the shear thickening is mild. We have not been able to reproduce discontinuous shear thickening, despite carrying out simulations above the freely-shearing packing fraction. We are led to the conclusion that *compressive* or *soft* particle roughness, as modelled by the various repulsion forces in the literature, is an important part of the discontinuous shear thickening model. This makes intuitive sense: if an increased flow rate can cause particles to be pushed closer together, the lubrication stresses between their surfaces will increase, causing the enhanced dissipation seen in shear thickening.

However, compressible roughness is not the only possible mechanism at the particle scale to potentially trigger macroscopic shear thickening. The stresses around particle contacts are extraordinarily high. It is possible that as particles separate, cavitation bubbles may form [33], breaking reversibility and causing additional dissipation. Equally, under sufficiently high pressures, the particle asperities may melt and fuse together. The contacting particles would then maintain contact until they overcome a critical force to separate – another source of energy dissipation. This latter mechanism may, indeed, require the fused particles to be modelled using the stick-rotate model of [19], which has been largely neglected since its original publication.

ACKNOWLEDGMENTS

We acknowledge financial support from EPSRC (EP/K502959/1) and Innovate UK (project number 132314). We would also like to thank Adam Burbidge and Alexander Morozov for their suggestions of alternative mechanisms for shear thickening.

[1] F R Dintzis, M A Berhow, E B Bagley, Y V Wu, and F C Felker, "Shear-thickening behavior and shear-induced structure in gently solubilized starches," Cereal Chemistry **73**, 638–643 (1996).

[2] M Wyart and M E Cates, "Discontinuous shear thickening without inertia in dense non-Brownian suspensions," Physical Review Letters **112**, 098302 (2014).

[3] Ryohei Seto, Romain Mari, Jeffrey F. Morris, and Morton M. Denn, "Discontinuous shear thickening of frictional hard-sphere suspensions," Physical Review Letters **111**, 218301 (2013).

[4] Eric Brown and Heinrich M. Jaeger, "Shear thickening in concentrated suspensions: Phenomenology, mechanisms, and relations to jamming," Reports on Progress in Physics **77**, 046602 (2014), arXiv:1307.0269.

[5] J F Brady and G Bossis, "Stokesian Dynamics," Annual Review of Fluid Mechanics **20**, 111–157 (1988).

[6] H A Barnes, "Shear-Thickening ("Dilatancy") in Suspensions of Nonaggregating Solid Particles Dispersed in Newtonian Liquids," Journal of Rheology **33**, 329–366 (1989).

[7] N Fernandez, R Mani, D Rinaldi, D Kadau, M Mosquet, H Lombois-Burger, J Cayer-Barrioz, H J Herrman, N D Spencer, and L Isa, "Microscopic mechanism for shear thickening of non-Brownian suspensions," Phys. Rev. Lett. **111**, 108301 (2013).

[8] C Heussinger, "Shear thickening in granular suspensions: Interparticle friction and dynamically correlated clusters," Phys. Rev. E **88**, 050201 (2013).

[9] B M Guy, M Hermes, and W C K Poon, "Towards a unified description of the rheology of hard-particle suspensions," Phys. Rev. Lett. **115**, 088304 (2015).

[10] N Y C Lin, B M Guy, M Hermes, C Ness, J Sun, W C K Poon, and I Cohen, "Hydrodynamic and contact contributions to continuous shear thickening in colloidal suspensions," Phys. Rev. Lett. **115**, 228304 (2015).

[11] C Clavaud, A Bérut, B Metzger, and Y Forterre, "Revealing the frictional transition in shear-thickening suspensions," Proceedings of the National Academiy of Sciences **114**, 5147–5152 (2017).

[12] J Comtet, G Chatté, A Niguès, L Bocquet, A Siria, and A Colin, "Pairwise frictional profile between particles determines discontinuous shear thickening transition in non-colloidal suspensions," Nature Communications **8**, 15633 (2017).

[13] Stany Gallier, Elisabeth Lemaire, François Peters, and Laurent Lobry, "Rheology of sheared suspensions of rough frictional particles," Journal of Fluid Mechanics **757**, 514–549 (2014).

[14] P A Arp and S G Mason, "The kinetics of flowing dispersions," Journal of Colloid and Interface Science **61**, 44–61 (1977).

[15] Shulin Zeng, Edward T Kerns, and Robert H Davis, "The nature of particle contacts in sedimentation," Physics of Fluids **8**, 1389–1396 (1996).

[16] Jeffrey R Smart and David T Leighton, "Measurement of the hydrodynamic surface roughness of noncolloidal spheres," Physics of Fluids A: Fluid Dynamics **1**, 52–60 (1989).

[17] Frédéric Blanc, François Peters, and Elisabeth Lemaire, "Experimental signature of the pair trajectories of rough spheres in the shear-induced microstructure in noncolloidal suspensions," Physical Review Letters **107**, 208302 (2011).

[18] F R Da Cunha and E J Hinch, "Shear-induced dispersion in a dilute suspension of rough spheres," Journal of Fluid Mechanics **309**, 211–223 (1996).

[19] Robert H Davis, "Effects of surface roughness on a sphere sedimenting through a dilute suspension of neutrally buoyant spheres," Physics of Fluids A: Fluid Dynamics **4**, 2607–2619 (1992).

[20] M L Ekiel-Jeżewska, F Feuillebois, N Lecoq, K Masmoudi, R Anthore, F Bostel, and E Wajnryb, "Hydrodynamic interactions between two spheres at contact," Phys. Rev. E **59**, 3182–3191 (1999).

[21] Romain Mari, Ryohei Seto, Jeffrey F. Morris, and Mor-

ton M. Denn, "Shear thickening, frictionless and frictional rheologies in non-Brownian suspensions," Journal of Rheology **58**, 1693–1724 (2014).

[22] Christopher Ness and Jin Sun, "Two-scale evolution during shear reversal in dense suspensions," Physical Review E **93**, 012604 (2016).

[23] M Trulsson, E DeGiuli, and M Wyart, "Effect of friction on dense suspension flows of hard particles," Physical Review E **95**, 012605 (2017).

[24] Adolfo Vázquez-Quesada, Roger I. Tanner, and Marco Ellero, "Shear thinning of noncolloidal suspensions," Physical Review Letters **117**, 108001 (2016).

[25] Helen J Wilson and Robert H Davis, "The viscosity of a dilute suspension of rough spheres," Journal of Fluid Mechanics **421**, 339–367 (2000).

[26] Helen J Wilson and Robert H Davis, "Shear stress of a monolayer of rough spheres," Journal of Fluid Mechanics **452**, 425–441 (2002).

[27] Helen J Wilson and Robert H Davis, "Shear stress of a monolayer of rough spheres—CORRIGENDUM," Journal of Fluid Mechanics **814**, 614–617 (2017).

[28] Sangtae Kim and Seppo J Karrila, *Microhydrodynamics: Principles and Selected Applications* (Dover Publications, Mineola, NY, USA, 2005).

[29] A Einstein, "Eine neue Bestimmung der Moleküldimensionen," Annalen der Physik **324**, 289–306 (1906).

[30] J F Brady and G Bossis, "The rheology of concentrated suspensions of spheres in simple shear-flow by numerical-simulation," J. Fluid Mech. **155**, 105–129 (1985).

[31] R. C. Ball and J. R. Melrose, "A simulation technique for many spheres in quasi-static motion under frame-invariant pair drag and Brownian forces," Physica A: Statistical Mechanics and its Applications **247**, 444–472 (1997).

[32] R Mari, R Seto, J F Morris, and M M Denn, "Nonmonotonic flow curves of shear thickening suspensions," Phys. Rev. E **91**, 052302 (2015).

[33] Po-Wen Yu, Steven L. Ceccio, and Grétar Tryggvason, "The collapse of a cavitation bubble in shear flows—A numerical study," Physics of Fluids **7**, 2608–2616 (1995).